Shape optimization of a submerged 2D hydrofoil and improvement of its lift-to-drag ratio using CFD-based mesh morphing-adjoint algorithm

Amin Nazemian[1], Parviz Ghadimi[2]✉, Aliakbar Ghadimi[3]

[1] https://orcid.org/0000-0001-6861-4488

[2] https://orcid.org/0000-0002-9315-5428

Amirkabir University of Technology, Dept. of Maritime Engineering
Hafez Ave, No 424, P.O. Box 15875-4413, Tehran, Iran
e-mail: [2]pghadimi@aut.ac.ir
✉ corresponding author

Abstract
Hydrofoils are utilized as instruments to improve the hydrodynamic performance of marine equipment. In this paper, the motion of a 2D NACA0012 hydrofoil advancing in water near the free surface was simulated, and a mesh morphing-adjoint based optimizer was used to maximize its lift-to-drag ratio. Ansys-Fluent was used as a CFD solver, and a mesh-morphing tool was used as a geometry reconstruction tool. Furthermore, the Adjoint solver was applied to evaluate the sensitivities of the objective function to all solution variables. Defined control points around the geometry are design variables that move in an appropriate direction through shape sensitivity. The computational results were validated against available experimental data and published numerical findings. Subsequently, different hydrodynamic characteristics of the optimized hydrofoil were compared to those of the original model at different angles of attack of 3, 3.5, 4, 4.5, 5, 5.5, 6, and 6.5°, and optimized shapes were determined. It was observed that the shape of the optimized hydrofoil was totally dependent on the angle of attack, which produced different lift-to-drag ratios. It is also seen that among higher angles of attack at which improvement in the *L*/*D* ratio became steady, the drag coefficient was the lowest at 5°. Therefore, it can be concluded that the appropriate angle of attack for a hydrofoil installation on the ship hull is 5°. Further investigation was conducted concerning the evolution of shape optimization, sensitivity analysis, free surface elevation, flow characteristics, and hydrodynamic performance of the hydrofoil at a 5° angle of attack.

Introduction

Hydrofoil sections are the most widely used and popular choice for lifting surfaces and are utilized as appendages in marine structures and light vehicles, such as autonomous underwater vehicles. Hydrofoils have been the focus of many past studies. Bai and Han (Bai & Han, 1994) studied flow around a two-dimensional hydrofoil under the influence of linear and nonlinear free surface conditions using the finite element method. Blasi et al. (Blasi et al., 2000) dealt with the practical study of wave-breaking behind submerged hydrofoils using the LDV method and showed that the downstream fluid was affected by the onset of shear flow and buoyancy forces. Daskovski (Daskovski, 2000) experimentally and theoretically studied the surface-approaching effect of the lift force created by an installed hydrofoil. Flipov (Flipov, 2001) analytically studied flow passing through hydrofoil using a perturbation

technique. Kouh et al. (Kouh, Lin & Chau, 2002) analyzed the hydrodynamic performance of a two-dimensional hydrofoil and the free surface effect. Rhee et al. (Rhee et al., 2003) examined the flow around a jet-controlled high-lift hydrofoil with a flap by applying both experimental and computational methods. They examined the applicability of using this technology as a control surface behind vessels. Bourgoyne (Bourgoyne, 2003) experimentally studied the vortices generated behind a 2D hydrofoil and measured the lift and drag forces. Hay and Visonneau (Hay & Visonneau, 2005) numerically simulated the free surface flow using an adaptive network and developed a new method to estimate water elevation. Carcaterra et al. (Carcaterra, Dessi & Mastroddi, 2005) analytically studied fluid-structure interactions and vibrations of elastic hydrofoil through a stochastic perturbation approach. Ducoin et al. (Ducoin et al., 2009) numerically examined the flow around a hydrofoil and analyzed boundary layer phenomena and flow separation. Zanette et al. (Zanette, Imbault & Tourabi, 2010) simulated flow around the blades of a water turbine and proposed a simplified design methodology for the structural analysis of blade sections. Guo et al. (Guo et al., 2012) examined the effect of a foil and interceptor on a catamaran's motions in still water. They evaluated the performance of a motion control system on improving the seakeeping behavior of a catamaran.

Wang et al. (Wang et al., 2017) studied two-dimensional and three-dimensional hydrofoils by using different optimization methods and optimized their performance based on changing the geometry by control points. Bonfiglio et al. (Bonfiglio et al., 2018) used regression and optimization to study the geometry of hydrofoil shape using numerical and experimental methods and optimized hydrofoil design parameters with respect to cavitation. Zhang et al. (Zhang, Yang & Liu, 2018) studied the creation of air bubbles in the body of a ship by placing a hydrofoil on the body and producing bubbles from it. They reduced this by a large amount of frictional resistance. Sacher et al. (Sacher et al., 2018) used the constrained EGO method to optimize the hydrofoil geometry with a flap to reduce drag and improve the performance under different sailing conditions. One of the most useful articles, which is the basis of our article, is Duncan's experiments for a NACA0012 submerged hydrofoil near the free surface at different depths and free surface wave patterns. Duncan (Duncan, 1983) conducted a series of experiments on a NACA0012 hydrofoil for various submergence depths, angles of attack, and Reynolds numbers.

He measured the free surface elevation and analyzed the effect of the mentioned parameters on the breaking wave. Duncan's experimental results were used as a validation case in this study. Based on the outlined literature review, one may conclude that an investigation of hydrofoil performance near the free surface requires more effort and study. Accordingly, the usage of an optimization process to increase its performance is appropriate. In this regard, the optimization of hydrofoil geometry near the free surface through CFD analysis is a crucial and challenging process because of the use of VOF and turbulence schemes and a hybrid mesh (a mix of triangular and quadrangular) (Nazemian & Ghadimi, 2020a).

The purpose of this study was to assess a mesh morphing-adjoint tool for the optimization of a fluid-exposed geometry in complex situations with a free surface, hybrid mesh, and curved geometry. The adjoint gradient-based solver provided sensitivity data from the CFD flow solution. Information obtained from the sensitivity field permitted the determination of the regions of the geometry where a small modification might create a large improvement in the quantity of interest. Adjoint-based optimization has been widely used in many industrial applications and disciplines like aerodynamics (Jameson, Martinelli & Pierce, 1998; Anderson & Venkatakrishnan, 1999), ground vehicles (Othmer, 2014; Muñoz-Paniagua, Garcia & Crespo, 2015), turbomachinery (Wang & He, 2010; He et al., 2019), and hydrofoil performance optimization (Garg et al., 2015; Garg et al. 2017).

Based on the outlined literature review, one may conclude that hydrofoils near the free surface have not been explored for optimization purposes. Furthermore, the optimization process of underwater complex geometries is a novel subject that uses mesh morphing geometry reconstruction and adjoint-based optimization. To examine a hydrofoil's performance near a free surface through optimization, Ansys-Fluent software was used as a solver, and a mesh-morphing tool was used as a geometry reconstruction tool. Accordingly, after validating the computed results, the analysis of a submerged hydrofoil at 0.21 cm depth from the free surface was performed at a 5° angle of attack, Froude number of 0.5672, and Reynolds number of 1.6e6, for which experimental data are available. RANSE equations were solved to analyze the flow, a VOF model was utilized to capture the free surface, and the mesh deformation capability by RBF-Morph was assessed to create a new geometry of the hydrofoil. This cycle of mesh deformation and shape optimization

continued until an optimum hydrofoil was obtained with the maximum lift-to-drag (L/D) ratio. Hydrofoils were examined at different angles of attack and lift and drag coefficients, and the optimized shapes of the examined hydrofoils were obtained. Further inquiry was performed in terms of the evolution of shape optimization, sensitivity analysis, free surface elevation, flow characteristics, and hydrodynamic performance of the hydrofoil at a 5° angle of attack, as an optimum hydrofoil shape.

Problem definition

A study of hydrodynamics and obtaining fluid flow around hydrofoils is a very important research area, especially in the marine industry. Hydrofoils are cross-sectional objects with a body designed to create a lifting force when passing through a fluid. There are two important functional parameters of hydrofoils, the lift and drag coefficients, which are non-dimensional parameters calculated by the following relations:

$$C_L = \frac{F_L}{\frac{1}{2}\rho V^2 c} \qquad (1)$$

$$C_D = \frac{F_D}{\frac{1}{2}\rho V^2 c} \qquad (2)$$

where F_L is the lift force per unit length, F_D is the drag force per unit length, and ρ is the fluid reference density. V is the upstream velocity, and c is the chord length of the hydrofoil, which is considered to be 20.3 cm. Figure 1 displays the profile of hydrofoil elements, which is a series of 4-digit NACA.

The numerical setup of the model was performed following the experiment conducted by Duncan (Duncan, 1983) at 0.8 m/s speed, a Froude number of 0.57, a Reynolds number of $1.6 \cdot 10^6$, and 5° angle of attack. The obtained results were compared against the reported experimental data at a 21 cm submergence depth. Shape optimization was performed on the hydrofoil. A 2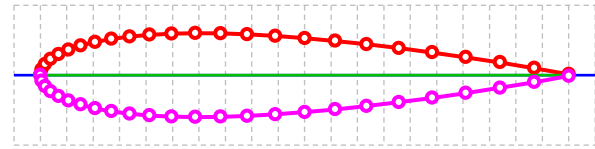D hydrofoil was modeled near the free surface. Optimization 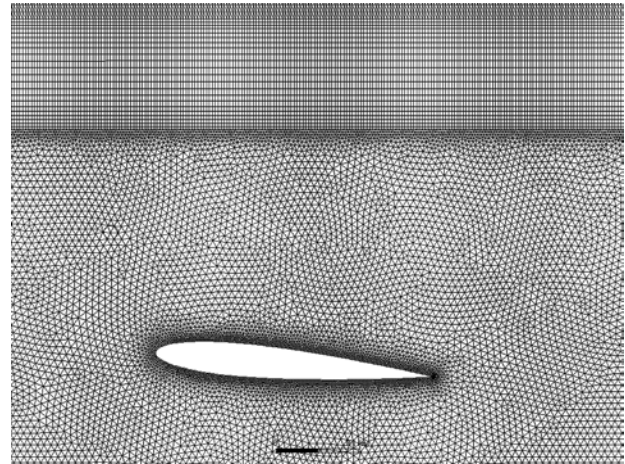was performed sequentially after verifying the reliability of the numerical simulation results. However, cavitation phenomena were not considered in the CFD model.

The computational domain was divided into two main regions. On the free surface, a structured mesh was used, while the rest of the domain was discretized using a triangular mesh. Figure 2 shows the domain gridding in which 250,000 cells were used for the computational domain. Boundary condition parameters were set with a 0.3% turbulent intensity and 0.001 for the turbulent viscosity ratio of the upstream flow. Velocity-pressure boundary conditions were employed for the unsteady implicit VOF method for the simulation. A uniform velocity for the velocity inlet boundary, pressure outlet for outlet boundary, and wall with slip conditions were employed at the top and bottom. No slip boundary conditions were used for the hydrofoil.

Meanwhile, the domain dimensions and geometry location of the hydrofoil are shown in Figure 3.
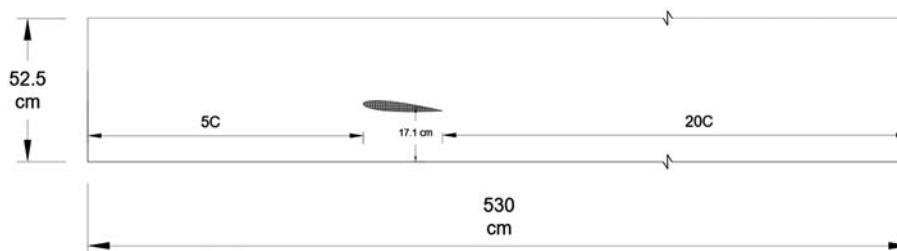

Figure 1. Hydrofoil NACA0012

Figure 2. Grid generation hydrofoil and free surface zone

Figure 3. Domain dimensions and hydrofoil position

Governing equations

Commercial CFD software Ansys-Fluent was used to simulate flow around the hydrofoil and the volume of fluid (VOF) scheme was used to capture the free surface. For incompressible flow without body forces, the averaged continuity and momentum equations in Cartesian coordinates can be written in tensor form as follows:

$$\frac{\partial(\rho\,\bar{u}_i)}{\partial x_i} = 0 \qquad (3)$$

$$\frac{\partial(\rho\,\bar{u}_i)}{\partial t} + \frac{\partial}{\partial x_j}\left(\rho\,\bar{u}_i\bar{u}_j + \rho\,\overline{u_i'u_j'}\right) = -\frac{\partial\bar{p}}{\partial x_i} + \frac{\partial\bar{\tau}_{ij}}{\partial x_j} \qquad (4)$$

where $\bar{\tau}_{ij}$ is the mean viscous stress tensor component, which is:

$$\bar{\tau}_{ij} = \mu\left(\frac{\partial\bar{u}_i}{\partial x_j} + \frac{\partial\bar{u}_j}{\partial x_i}\right) \qquad (5)$$

where p is the mean pressure, $\bar{u}_i$ is the averaged Cartesian components of the velocity vector, $\rho\,\overline{u_i'u_j'}$ is the Reynolds stress, ρ is the fluid density, and μ is the dynamic viscosity.

To model the fluid flow, the solver employed the finite volume method which discretized the integral formulation of the Navier-Stokes equations. The RANSE solver employed a predictor-corrector approach to link the continuity and momentum equations. The turbulence model selected in this study was a standard k-ε model, which has been extensively used for industrial applications (Nazemian & Ghadimi, 2021). To numerically capture the free surface, the VOF scheme was used. Through this approach, the volume fraction c was defined as the ratio of the volume of air in the cell to the total volume of the cell (V_{air}/V_{total}), and the fluid density ρ and viscosity μ were calculated as:

$$\rho = \rho_{air}\,c + \rho_{water}\,(1 - c) \qquad (6)$$

$$\mu = \mu_{air}\,c + \mu_{water}\,(1 - c) \qquad (7)$$

Optimization algorithm

Optimization of fluid-exposed geometries is a crucial issue in computational fluid dynamics. Mesh morphing allows the optimization of various and complex geometries without rebuilding and applying manual changes in each optimization step. This feature has the benefit of less computational time and can handle large and complex grids while maintaining mesh consistency and quality. Furthermore,

Figure 4. Mesh morphing region around the hydrofoil geometry

the adjoint solver determines the sensitivity of an objective with respect to the user-specified control variables. The adjoint solver identifies the most influential variables that make significant changes in the objective function. The calculation objective of this study was the lift-to-drag ratio of an underwater hydrofoil near the free surface, which was calculated by the RANSE-based CFD solver on morphed meshes. Surface mesh is deformed through mesh morphing and the morphing is applied to all domain mesh, smoothly (Biancolini et al. 2013). Ultimately, the obtained RBF solution was sent to the RANS solver. The mesh morphing tool was with Fluent commercial software and is known as RBF-Morph (Petrone, Hill & Biancolini, 2014; Biancolini, 2017). For the target problem, the aforementioned deformation regions are shown in Figure 4. The number of these points is 14×14 in the x and y-axis, respectively. Accordingly, a rectangular control volume enclosed the boundary whose shape needed to be modified. To keep the hydrofoil dimensions constant and restrict huge deformations, the box was set tangentially to the geometry. The scaling factor that controls the magnitude of the shape modification was set to 0.1. This value prevents substantial deformation, resulting in a negative mesh volume during the optimization process. In addition, the mesh quality remained, and the deformation was gradually implemented in a continuous and smooth way.

Mesh morphing was applied iteratively to the geometry. Adjoint solvers take a CFD flow solution and calculate the sensitivity of performance indicators (L/D ratio) for all design variables. The objective function depends on both flow-field variables u and the control point of body x. Then:

$$\text{Objective function}: J[u(x), x] \qquad (8)$$

where J is the objective function, and $\vec{x}$ is the vector of the design variables. To maximize the J gradients, $\partial J/\partial x$ should be computed (Biancolini, 2017). The main adjoint-based solver formula for the objective of L/D is:

$$\delta J\left(\frac{L}{D}\right) = \sum_{Mesh} w^n \cdot \delta\,\vec{x}^n \qquad (9)$$

where w represents the shape sensitivity of the observed value with respect to (wall boundary) grid

node locations, and n is the number of design variables. The sign of δ in the formula shows variations in the parameters. The displacement of mesh nodes was computed according to Eq. (9).

Formulation of the optimization problem

The objective of the study is the L/D of a 2D hydrofoil exposed to a uniform constant velocity flow beneath the free surface. $J(x)$ is the objective function, and x is the vector of design variables, known as mesh morphing control points. If the optimal candidate at the iteration $i + 1$ is x_{i+1}, this can be defined based on a former design x_i as indicated by:

$$x_{i+1} = x_i + \alpha_i\, S_i \qquad (10)$$

where α_i is the step size in the search direction S_i. To recognize the search direction, a first-order gradient was calculated via the finite difference approach. This function computed the difference in the displacement between cell centers of the initial mesh and the desired point of the source grids.

$$S_i = -\nabla J\big(x_i\big) \qquad (11)$$

$$\frac{dJ}{dx_k} = \left[\frac{J\big(x_k + \Delta x_k\big) - J\big(x_k\big)}{\Delta x_k}\right] \quad k = 1\ldots n \quad (12)$$

Performing numerical computations of an objective function's gradients for a complex system can be a complicated task, especially if the number of design parameters is large and the objective function evaluation constitutes an expensive effort. To reduce the computational cost of calculating dJ/dx_k, an adjoint approach is presented. The cost of determining the gradient is directly proportional to the number of variables used to define the problem. Thus, the hydrodynamic shape optimization based on these approaches requires intensive computational efforts and fast CPUs. The most cost-effective technique is to compute the gradient by solving an adjoint problem. Therefore, the objective function depends on both flow-field variables (u) and the control point of a body, (x). The Ansys-Fluent adjoint solver was adopted for the current problem. The formulation of the discrete adjoint method is briefly described in the next section.

Formulation of Discrete Adjoint Method

As pointed out earlier, the minimization of J requires the computation of the gradient. The objective function depends on both the design variable

and flow field variables $J(u(x), x)$ and is subject to the constraint and the discrete governing equations $N(u(x), x) = 0$, which must be all satisfied. Therefore:

$$\frac{dJ}{dx_k} = \frac{\partial J}{\partial u}\frac{du}{dx_k} + \frac{\partial J}{\partial x_k} \qquad (13)$$

which is subject to the following constraint:

$$\frac{\partial N}{\partial u}\frac{du}{dx_k} + \frac{\partial N}{\partial x_k} = 0 \qquad (14)$$

In Eq. (13), the challenge for determining the sensitivity of an objective function with respect to the design variables is that changing the latter parameters caused a change in the flow variables, which indirectly changed the objective function. The adjoint method provides a mechanism for replacing the first term of Eq. (13) by an expression that depends only on x_k. This implies that the adjoint method eliminates the specific changes that occur in the flow whenever the design variables are modified. From Eq. (14), the following relation is obtained:

$$\frac{du}{dx_k} = -\left[\left(\frac{\partial N}{\partial u}\right)^{-1}\frac{\partial N}{\partial x_k}\right] \qquad (15)$$

By introducing Eq. (15) into Eq. (11) and regrouping, the following formula was obtained:

$$\frac{dJ}{dx_k} = \frac{\partial J}{\partial u}\left\{-\left[\left(\frac{\partial N}{\partial u}\right)^{-1}\frac{\partial N}{\partial x_k}\right]\right\} + \frac{\partial J}{\partial x_k} =$$
$$= \left[-\frac{\partial J}{\partial u}\left(\frac{\partial N}{\partial u}\right)^{-1}\right]\frac{\partial N}{\partial x_k} + \frac{\partial J}{\partial x_k} \qquad (16)$$

By using the Lagrange multiplier λ, the resulting calculation of the sensitivity of J is given as:

$$\frac{dJ}{dx_k} = -\lambda^T\frac{\partial N}{\partial x_k} + \frac{\partial J}{\partial x_k} \qquad (17)$$

where λ^T is the vector of adjoint variables (Lagrange multipliers). λ^T is chosen to satisfy:

$$\frac{\partial J}{\partial u} = \lambda^T\frac{\partial N}{\partial u} \qquad (18)$$

which is called the adjoint equation, which is defined by the current state of the flow and does not depend on x_k. Therefore, for determining x_k, it is necessary to call both CFD and adjoint equation solvers. The cost of solving the adjoint equation is comparable to that of solving the flow equation. Information obtained from the sensitivity field permits the determination of the geometry regions where a small modification might considerably improve the quantity of interest.

Mesh sensitivity

To find an optimum mesh size, the lift and drag coefficients of numerical simulations were used, and the results of submerged hydrofoil characteristics at an angle of attack of 5° and speed of 0.8 m/s are shown in Table 1. The number of elements in three conditions of domain gridding was analyzed. Figure 5 shows the lift and drag coefficients as a function of the mesh size. It is obvious that 250K elements was the appropriate mesh size, which was adopted for further studies.

Table 1. Lift and drag coefficients in different solution cases

Case No.	Mesh	Element No.	Lift coef. (C_L)	Drag coef. (C_D)
1	Coarse	128K	0.540	0.0225
2	Medium	250K	0.562	0.0237
3	Fine	440K	0.565	0.0242

Validation

Free surface elevation

For validation, existing experimental data (Duncan, 1983) were utilized, as previously described.

Figure 5. Lift and drag coefficient versus the number of elements

The simulations exactly matched the Duncan study at flow speed 0.8 m/s and hydrofoil's angle of attack of 5°. Figure 6 displays the computed wave profiles on the free surface along with the experimental data. The numerical results were compared with the experimental data (Duncan, 1983) in the form of free surface elevation. Figure 7 shows the volume fraction contour and the wave generated by the submerged hydrofoil.

The *x*-axis in Figure 6 starts from the leading edge of the hydrofoil. As evident in Figure 6,

Figure 6. Comparison of the computed free surface elevation with experimental data (Duncan, 1983)
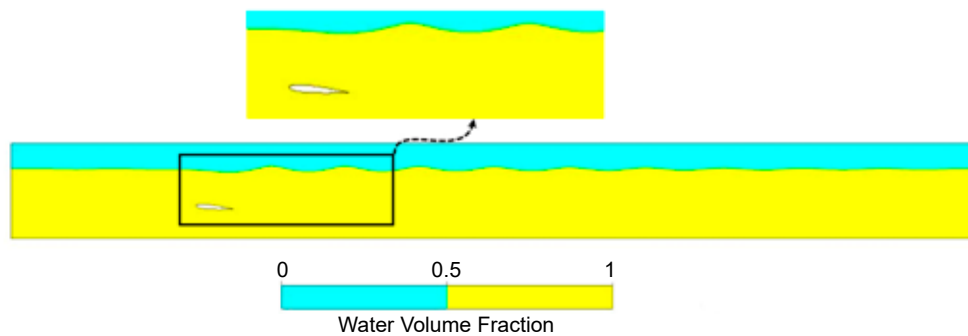
Figure 7. Volume of fraction contour and wave profile
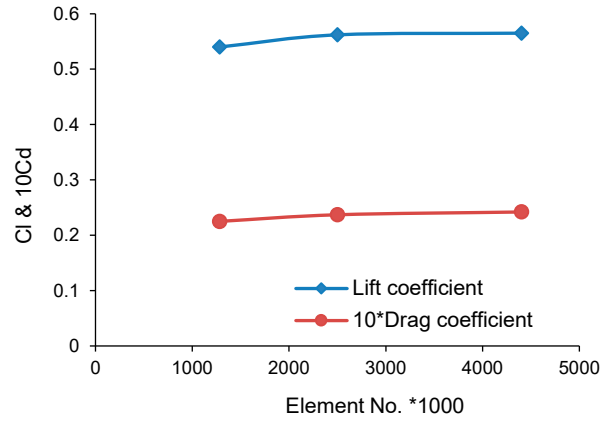
a comparison between CFD simulation and experiment results illustrates relatively good agreement. To further validate the results of this study, similar conditions of the numerical work conducted by Raza et al. (Raza et al., 2013) were simulated and compared. The comparison illustrated that the error of the lift coefficient was 4.7%, while it was 12.2% for the drag, which showed relatively good agreement.

Results and discussion

This study focuses on the shape optimization of a submerged hydrofoil near the free surface to reduce the resistance of ships. An accurate and rapidly-converged optimization cycle was introduced based on conditions similar to Duncan's experiment (Duncan, 1983). First, the optimization process results were analyzed for different angles of attack (3°, 4°, 5°, 6°). At each angle of attack, the adjoint-based optimization is applied separately. Second, the history of shape optimization evolution of hydrofoil is prescribed in the following subsection.

Shape optimization of hydrofoil at different angles of attack

The optimization process was applied for an operational range of angles of attack for ship hull hydrofoils (Guo et al., 2012; Raza et al., 2013). A higher angle of attack increased the ship's appendage resistance and was not applicable for marine vehicles. Hydrofoil shapes, before and after optimization, were also analyzed at different angles of attack [3, 3.5, 4, 4.5, 5, 5.5, 6, 6.5] degrees. The results of this analysis for angles of attack of 3, 4, 5, and 6° are shown in Figure 8.

In Figure 8, changes in the hydrofoil geometry are shown, considering the least geometric variation, while achieving the highest lift-to-drag coefficient. By this changing process, it can be observed that optimization at each angle provided a different geometry shape, and the change in the trailing edge region was the highest. It also shows that this region is highly sensitive to the hydrodynamic performance of the hydrofoil. To better understand the free surface condition, plots of the generated free surface
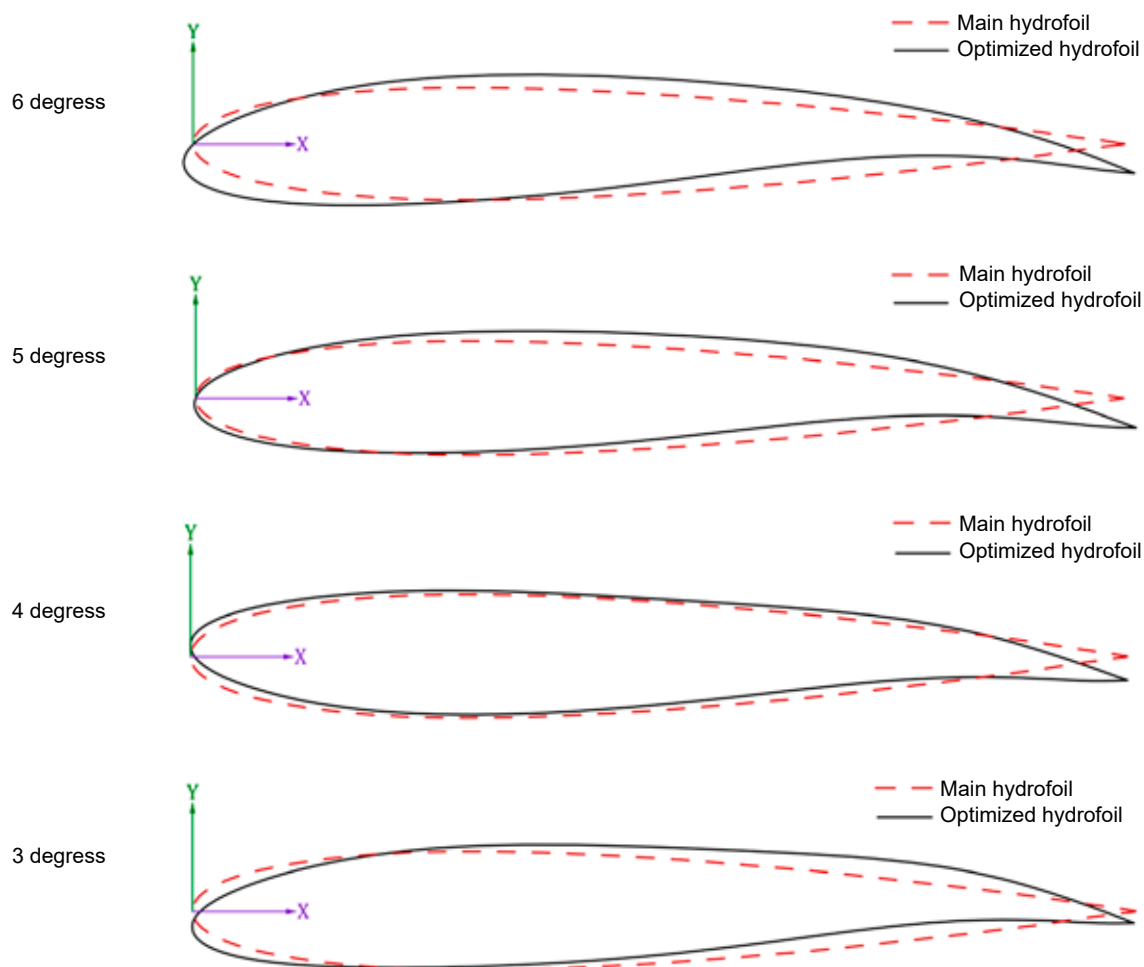

Figure 8. Geometry modification at different angles of attack [3, 4, 5, and 6°]
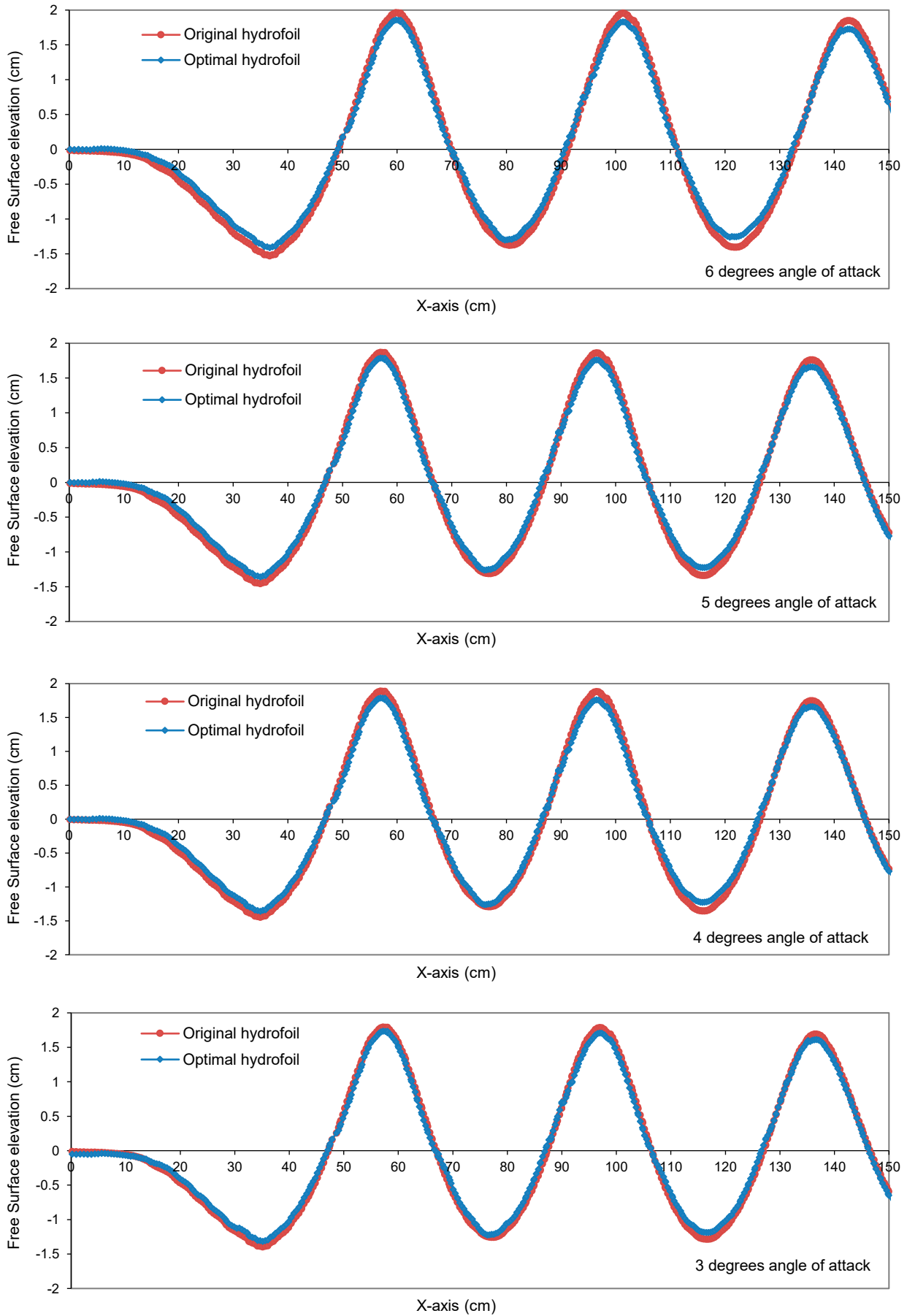
Figure 9. Free surface elevation at different angles of attack [3, 4, 5, and 6°] for the original and optimal hydrofoils

Table 2. Lift and drag coefficients of the main and optimized hydrofoils at different angles of attack

Angle of attack	Main hydrofoil			Optimized hydrofoil			Improvement in L/D
	Lift coef. (C_L)	Drag coef. (C_D)	L/D	Lift coef. (C_L)	Drag coef. (C_D)	L/D	Percentage of L/D increase
3°	0.3035	0.0197	15.36	0.6256	0.022	28.2	83.6%
4°	0.4039	0.0206	19.6	0.7915	0.0254	31.16	58.98%
5°	0.5623	0.0237	23.71	1.023	0.0283	36.16	56.2%
6°	0.6337	0.0248	25.52	1.174	0.031	36.8	44.2%

profiles are illustrated in Figure 9, which correspond to both original and optimal hydrofoils at different angles of attack.

Figure 9 indicates that changing the hydrofoil geometry has a small effect on the free surface elevation. However, at a 6° angle of attack, the wave period is a little different from the other angles. Lift and drag coefficients and L/D ratios for angles of attacks of 3, 4, 5, and 6° in the two studied states are shown in Table 2, and a comparison of the L/D ratios at angles of attack of 3, 3.5, 4, 4.5, 5, 5.5, 6, and 6.5° are illustrated in Figure 10. This was done to better understand the L/D ratio at other angles of attack.
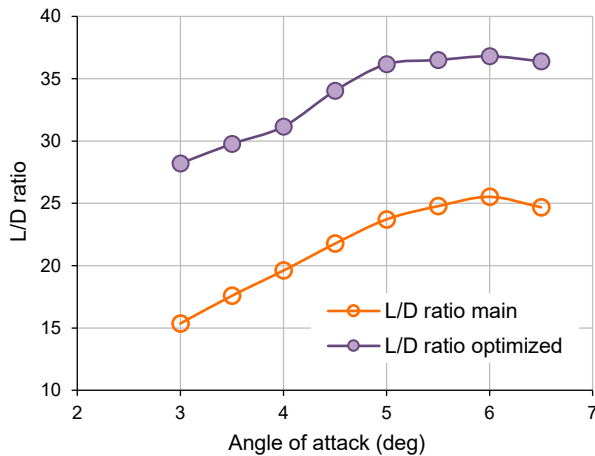
Figure 10. Lift-to-drag ratio for different angles of attack

As observed in Figure 10, there was a substantial increase in the L/D ratio of up to 5°. Subsequently, the variation in L/D at 5° to 6.5° was not large, and beyond 6.5° angle of attack, the graph of L/D was a straight line showing a small decrease. Furthermore, Table 2 shows that among higher angles of attack, the drag coefficient was the lowest at 5°, which is desirable. Therefore, one may assume that an appropriate angle of attack for a hydrofoil installation on a ship hull is 5° (Guo et al., 2012; Duncan, 1983). Accordingly, further investigation of the hydrofoil regarding the evolution of its shape optimization, sensitivity analysis, free surface elevation,

flow characteristics, and hydrodynamic performance was conducted at a 5° angle of attack.

History of shape optimization evolution, sensitivity analysis, free surface elevation, flow characteristics, and hydrodynamic performance

Numerical simulations of the uniform flow at a 0.8 m/s velocity for a 5° angle of attack were conducted, and after CFD validation, adjoint optimization was started. Subsequently, the sensitivity information was obtained from the adjoint solver for the defined observable. This information was used to introduce the first deformation of the hydrofoil. Six successive optimization steps were performed. Each of the generated geometries was simulated until convergence was achieved for a 10% L/D increase.

History of shape optimization evolution

The evolution of the lift-to-drag ratio from the initial design is plotted in Figure 11. At the end of the optimization process, a 56.2% improvement in the L/D was achieved. It is important to note that the geometry improvement continued until adjoint convergence was achieved in the optimization process. Meanwhile, sensitivity contours play important role in decision-making, which is explained in the next subsection.
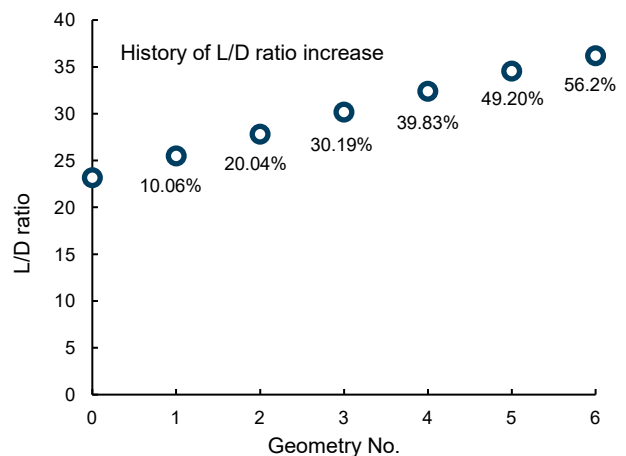
Figure 11. History of lift-to-drag ratio increase at a 5° angle of attack

Sensitivity analysis

Adjoint optimization explores the sensitivity of an objective on the surface of the geometry, which is hereby the lift-to-drag ratio. The acquired optimum hydrofoil and the original shape for a 5° angle of attack is depicted in Figure 12.

The comparison graph reveals that most changes occurred in the trailing edge region because this region is highly sensitive to the lift-to-drag ratio. The adjoint pressure or sensitivity to mass source field for the initial geometry is presented in Figure 13.

This field can be interpreted as the sensitivity of an observable with respect to mass sources or sinks in the domain (RBF, 2022). In other words, this field indicates the effect of the addition or removal of a fluid (mass flow rate per unit volume) from the domain upon the objective, and it leads to surface deformation. In fact, the adjoint solution field provides useful insight into regions of the flow domain where the observation of interest is potentially sensitive to the particular features of the mesh and discretization

process that affect the local mass balance (Nazemian & Ghadimi, 2020b; RBF, 2022).

Another important post-processing method for sensitivity results is sensitivity to shape vector analysis. This plot helps understand how to change the design to increase its sensitivity. Figure 14 displays the two-dimensional sensitivity of the shape vector on the objective.

Figure 14 shows how sensitive the lift-to-drag ratio on the submerged hydrofoil is to changes in the surface shape. The *L/D* ratio is affected more significantly if the hydrofoil geometry is deformed on the upper surface rather than the lower surface of the hydrofoil. The shape sensitivity plot of 2D vectors defines the optimal displacement of geometric variables for a suitable modification.

Free surface elevation

The free surface elevation for both the original and optimized hydrofoil (step 6) is presented in Figure 15 at a 5° angle of attack. As seen in Figure 15,
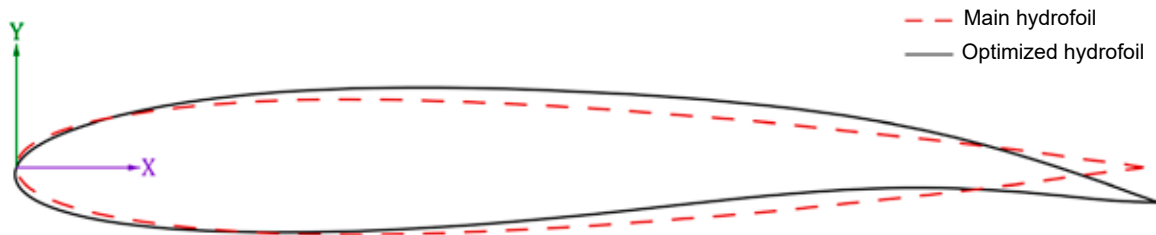

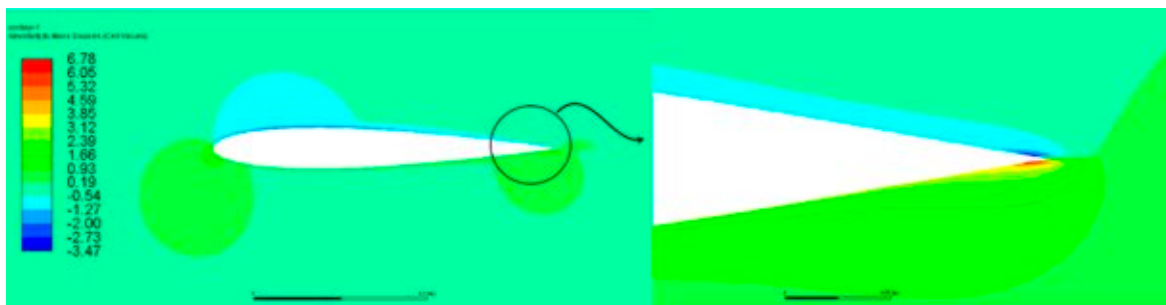**Figure 12. Modified shape of the submerged hydrofoil NACA0012 at a 5° angle of attack**

Figure 13. Adjoint pressure or sensitivity to mass source fields for an initial hydrofoil based on an objective lift-to-drag ratio
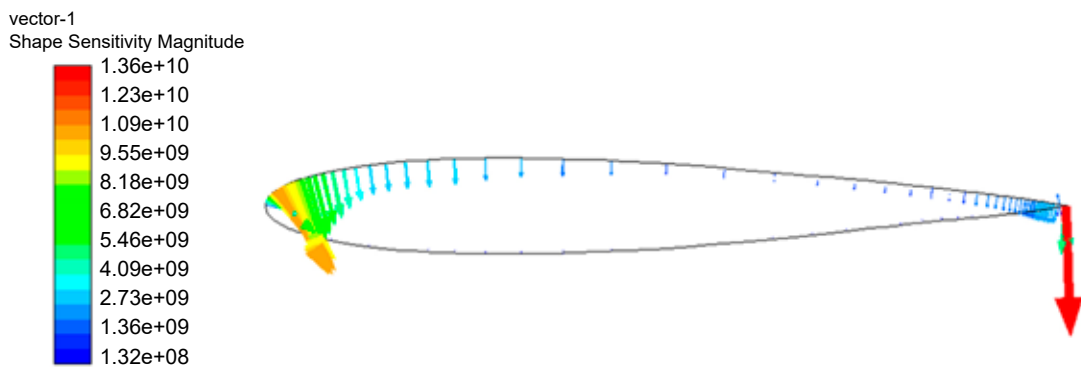

Figure 14. Adjoint sensitivity of shape 2D vector for initial hydrofoil based on the objective lift-to-drag ratio
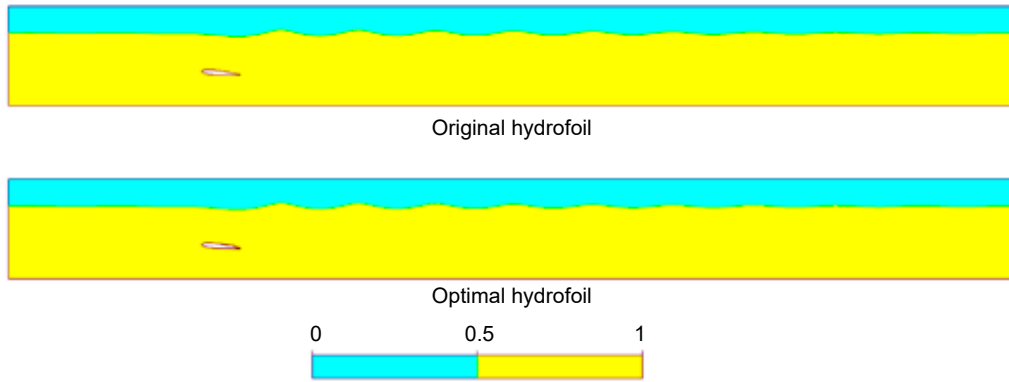
Figure 15. Free surface elevation for the original and optimized NACA0012 hydrofoil at a 5° angle of attack

there is not a remarkable change in the free surface behavior for either the original or optimal hydrofoil.

Flow characteristics

The pressure and velocity contours of the original and optimized hydrofoil at a 5° angle of attack are demonstrated in Figures 16 and 17. These plots present the main flow characteristics of the underwater structure.

As observed in Figure 16, pressure contours in the optimized hydrofoil displayed larger values than those in the original hydrofoil. The higher difference between the leading edge and trailing edge creates a strong force that results in higher lift and drag forces. The velocity contours demonstrate the same behavior for the optimized hydrofoil, as shown in Figure 17. Plots of the streamline around the original shape of the NACA0012 hydrofoil and its optimized shape are also illustrated in Figure 18.

For the optimized hydrofoil in Figure 18, the flow direction in the downstream area shows a more vertical direction, i.e., the angle between the inlet and outlet flow direction is larger than in the original state.
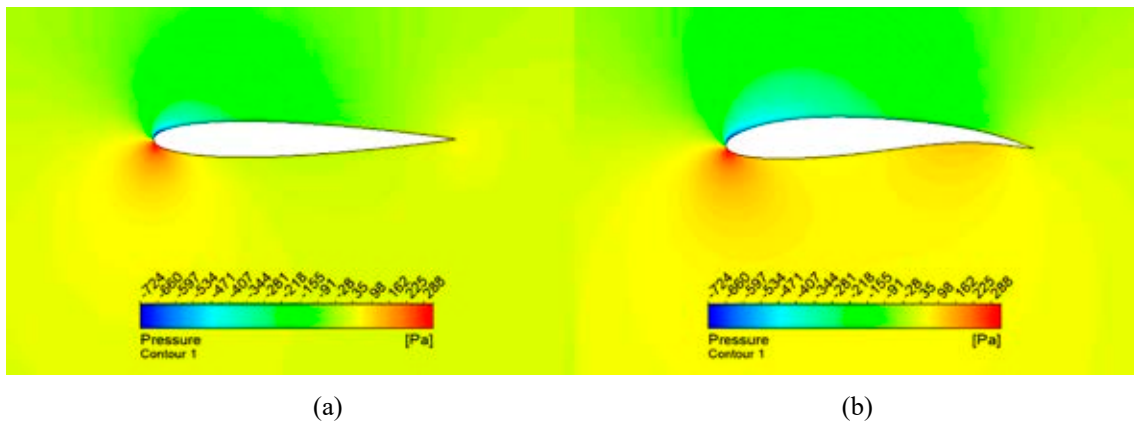

(a) (b)

Figure 16. Pressure contours of the original (a) and optimized (b) hydrofoils at a 5° angle of attack
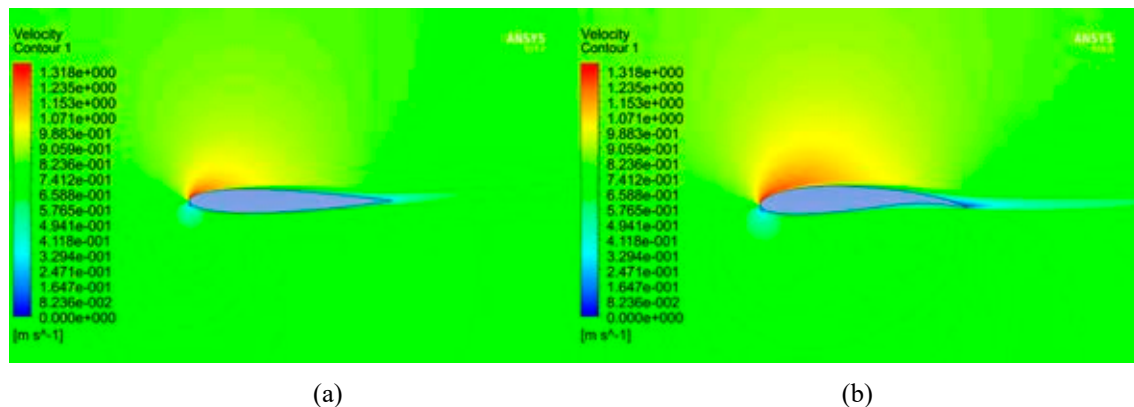

(a) (b)

Figure 17. Velocity contours of the original (a) and optimized (b) hydrofoils at a 5° angle of attack
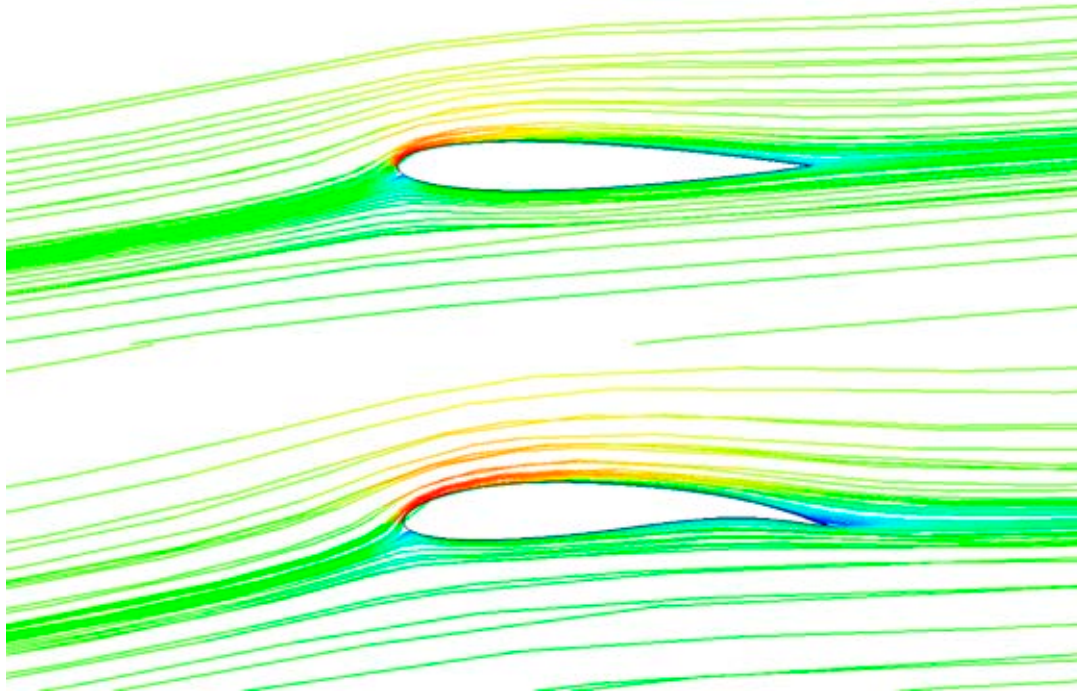
Figure 18. Streamline fluid around main and optimized hydrofoil at a 5° angle of attack

Hydrodynamic performance

Comparison of the initial and optimized geometries assists the analysis of the evolution of the hydrofoil during optimization. A comparison of the lift and drag coefficients between the original and optimal hydrofoils at a 5° angle of attack shows an improvement in the hydrofoil. Accordingly, the lift coefficient of the original hydrofoil was 0.562, which improved to 1.023. However, the drag coefficient increased from 0.0237 to 0.0283. Although the drag coefficient increased by about 8%, the lift coefficient increased by about 40%. A comparison of the lift-to-drag ratio between both the original and optimal hydrofoil at a 5° angle of attack is shown in Figure 19.

As evident in Figure 19, the lift-to-drag ratio for the main hydrofoil was 23.71, which increased to
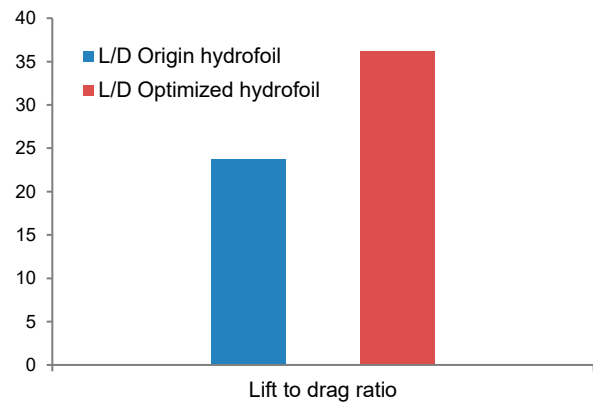

Figure 19. Comparison of the lift-to-drag ratio between the original and optimal hydrofoil

36.16 after shape optimization of the hydrofoil. Thus far, optimization of hydrofoil has been done only at
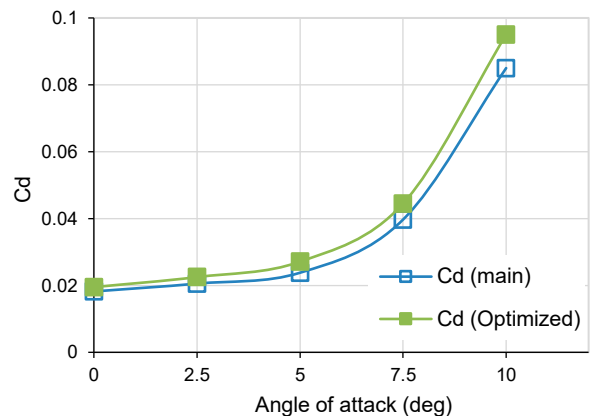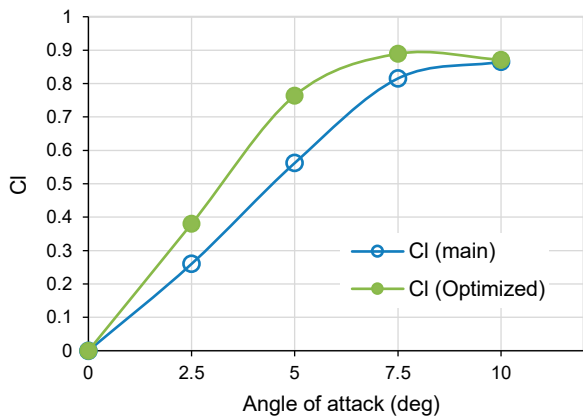

Figure 20. (a) Lift and (b) drag coefficient of hydrofoil at different angles of attack

an angle of 5°. In order to gain a better understanding of the hydrodynamic performance of the hydrofoil, the lift and drag coefficients of both original and optimized hydrofoils were examined at other angles of attack and are displayed in Figure 20.

According to Figure 20, the lift coefficient increased at a 5° angle of attack, but at higher angles of attack, little change was observed, and the lift coefficient in the original and optimal hydrofoil remained nearly the same. However, at higher angles, the drag force was greater than at lower angles of attack. Figure 21, which is the main chart for the hydrofoil hydrodynamic performance, shows the lift-to-drag force ratio.
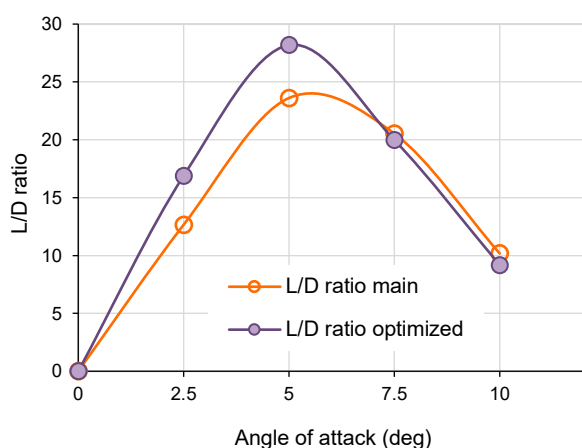

Figure 21. Lift-to-drag ratio (*L/D*) of the hydrofoil at different angles of attack

An upward trend was observed in the lift-to-drag ratio for angles of attack ranging from 0 to 5° in Figure 21. As a result of optimization, the maximum improvement in the lift-to-drag ratio was obtained at a 5° angle of attack, but this ratio slightly decreased beyond 7.5°.

Conclusions

Hydrofoils are lifting surface tools with different applications in the marine industry. Hydrofoils operate under different conditions, especially near free surfaces. For this purpose, it is necessary to study the hydrodynamic performance of a submerged hydrofoil near the free surface. In this paper, the fluid flow around a two-dimensional NACA0012 hydrofoil was simulated by the commercial CFD software, Ansys-Fluent. RANSE equations were considered along with turbulent flow conditions and the VOF method for a multiphase problem. The numerical results were compared with the available experimental and numerical data, and good compliance was

achieved. Subsequently, the geometry of the considered hydrofoil was optimized by the adjoint solver tool using GUI fluent software. A CFD-based solver was used to assess the hydrodynamic performance of the hydrofoil, and a mesh-morphing tool was used as a geometry reconstruction tool. An iterative operation was adopted to increase the lift-to-drag ratio of the hydrofoil. This modification process was applied for different angles of attack, and a clear improvement in the *L/D* ratio at each angle of attack was observed, but the outcome was different. For example, at a 3° angle of attack, the improvement in the *L/D* ratio was 83.6%, while at 5°, the improvement was 56.2%. It was also observed that among higher angles of attack at which the improvement in the *L/D* ratio was high and became steady, the drag coefficient was the lowest at 5°.

Therefore, one may conclude that the most suitable angle of attack for a hydrofoil installation on the ship hull is 5°. Further investigation was performed about the evolution of shape optimization, sensitivity analysis, free surface elevation, flow characteristics, and hydrodynamic performance of the hydrofoil at a 5° angle of attack. Accordingly, improvements in the hydrofoil geometry were analyzed by the sensitivity data. The mass to source contour and vector field of the shape sensitivity on the objective indicated the appropriate modification of the submerged hydrofoil. Based on the obtained results, one may also conclude that combining a CFD-based adjoint solver and mesh morphing technology is an effective optimization tool for complex fluid-exposed geometries with various domain gridding.

The capability and advantage of adjoint-morphing tools for design studies can be further explored for various hydrofoil operational conditions such as depth ratio effectiveness and three-dimensional effects in future studies. Besides, the real conditions of hydrofoil operation are always accompanied by cavitation phenomena, which affect the hydrodynamic performance. Further studies will be conducted about the shape optimization of hydrofoils by considering cavitation.

References

1. Anderson, W.K. & Venkatakrishnan, V. (1999) Aerodynamic design optimization on unstructured grids with a continuous adjoint formulation. *Computers & Fluids* 28(4–5), pp. 443–480, doi: 10.1016/S0045-7930(98)00041-3.
2. Bai, K.J. & Han, J.H. (1994) A localized finite element method for the non-linear steady waves due to a two-dimensional hydrofoil. *Journal of Ship Research* 38 (01), pp. 42–51, doi: 10.5957/jsr.1994.38.1.42.

3. Biancolini, M.E. (2017) *Fast Radial Basis Functions for Engineering Applications*. Springer, Cham.

4. Biancolini, M.E., Cella, U., Travostino, G. & Mancini, M. (2013) Shaping up – Mesh morphing reduces the time required to optimize an aircraft wing. *ANSYS Advantage Magazine* VII, 1.

5. Blasi, P.D., Romano, G.P., Felice, F.D. & Lalli, F. (2000) Experimental study of breaking wave flow field past a submerged hydrofoil by LDV. *International Journal of Offshore and Polar Engineering* 10(4), pp. 263–269.

6. Bonfiglio, L., Perdikarisa, P., Brizzolara, S. & Karniadakis, G.E. (2018) Multi-fidelity optimization of super-cavitating hydrofoils. *Computer Methods in Applied Mechanics and Engineering* 332, pp. 63–85, doi: 10.1016/j.cma.2017.12.009.

7. Bourgoyne, D.A. (2003) *Flow over a hydrofoil with trailing edge vortex shedding at high Reynolds number*. Ph.D. Thesis, Mechanical Engineering, University of Michigan.

8. Carcaterra, A., Dessi, D. & Mastroddi, F. (2005) Hydrofoil vibration induced by a random flow: A stochastic perturbation approach. *Journal of Sound and Vibration* 283 (1–2), pp. 401–432, doi: 10.1016/j.jsv.2004.04.040.

9. Daskovsky, M. (2000) The hydrofoil in surface proximity, theory and experiment. *Ocean Engineering* 27 (10), pp. 1129–1159, doi: 10.1016/S0029-8018(99)00032-3.

10. Ducoin, A., Astolfi, J.A., Deniset, F. & Sigrist, J.-F. (2009) Computational and experimental investigation of flow over a transient pitching hydrofoil. *European Journal of Mechanics – B/Fluids* 28 (6), pp. 728–743, doi: 10.1016/j.euromechflu.2009.06.001.

11. Duncan, J.H. (1983) The breaking and non-breaking wave resistance of a two-dimensional hydrofoil. *Journal of Fluid Mechanics* 126 (1), pp. 507–520, doi: 10.1017/S0022112083000294.

12. Filippov, S.I. (2001) Flow past a submerged hydrofoil. *Fluid Dynamics* 36(3), pp. 489–496, doi: 10.1023/A:1019200521581.

13. Garg, N., Kenway, G.K.W., Lyu, Z., Martins, J.R.R.A. & Young, Y.L. (2015) High-fidelity hydrodynamic shape optimization of a 3-D hydrofoil. *Journal of Ship Research* 59 (4), pp. 209–226, doi: 10.5957/jsr.2015.59.4.209.

14. Garg, N., Kenway, G.K.W., Martins, J.R.R.A. & Young, Y.L. (2017) High-fidelity multipoint hydrostructural optimization of a 3-D hydrofoil. *Journal of Fluids and Structures* 71, pp. 15–39, doi: 10.1016/j.jfluidstructs.2017.02.001.

15. Guo, Z., Lin, Z., Yang, Q. & Li, X. (2012) Research of Combined Control Scheme for Fast Catamaran Motion Control Using T-foils and Interceptors. *International Journal of Intelligent Engineering & Systems* 5 (2).

16. Hay, A. & Visonneau, M. (2005) Computation of free-surface flows with local mesh adaptation. *International Journal for Numerical Methods in Fluids* 49 (7), pp. 785–816.

17. He, P., Martins, J.R.R.A., Mader, C.A. & Maki, K. (2019) Aerothermal optimization of a ribbed U-bend cooling channel using the adjoint method. *International Journal of Heat and Mass Transfer* 140, pp. 152–172.

18. Jameson, A., Martinelli, L. & Pierce, N.A. (1998) Optimum aerodynamic design using the Navier–Stokes equations. *Theoretical and Computational Fluid Dynamics* 10 (1), pp. 213–237, doi: 10.1007/s001620050060.

19. Kouh, J.-S., Lin, T.J. & Chau, S.-W. (2002) Performance analysis of two-dimensional hydrofoil under free surface. *Journal of National Taiwan University* 86.

20. Muñoz-Paniagua, J., Garcia, J. & Crespo, A. (2015) Aerodynamic Optimization of the Nose Shape of a Train Using the Adjoint Method. *Journal of Applied Fluid Mechanics* 8 (3), pp. 601–612, doi: 10.18869/acadpub.jafm.67.222.22632.

21. Nazemian, A. & Ghadimi, P. (2020a) Shape optimization of a hydrofoil with leadingedge protuberances using full factorial sweep sampling and an RBF surrogate model. *Scientific Journals of the Maritime University of Szczecin, Zeszyty Naukowe Akademii Morskiej w Szczecinie* 62 (134), pp. 116–123, doi: 10.17402/426.

22. Nazemian, A. & Ghadimi, P. (2020b) Shape optimization of trimaran ship hull using CFD-based simulation and adjoint solver. *Ships and Offshore Structures*, doi: 10.1080/17445302.2020.1827807.

23. Nazemian, A. & Ghadimi, P. (2021) Automated CFD-based optimization of inverted bow shape of a trimaran ship: An applicable and efficient optimization platform. *Scientia Iranica* 28 (5 B), pp. 2751–2768.

24. Othmer, C. (2014) Adjoint methods for car aerodynamics. *Journal of Mathematics in Industry* 4 (6), 6, doi: 10.1186/2190-5983-4-6.

25. Petrone, G., Hill, D.C. & Biancolini, M.E. (2014) *Track by Track Robust Optimization of a F1 Front Wing using Adjoint Solutions and Radial Basis Functions*. 44th AIAA Fluid Dynamics Conference, Atlanta, Georgia (USA).

26. Raza, N., Mehmood, I., Rafuddin, H., Bilal, S. & Rafque, M. (2013) *Numerical simulation of free surface effect on moving hydrofoil near free surface*. 10th International Bhurban Conference on Applied Sciences & Technology (IBCAST), Islamabad, Pakistan.

27. RBF (2022) RBF-Morph™, Webinars and Q&A [Online] Available from: http://www.rbf-morph.com, [Accessed: January 02, 2022].

28. Rhee, S.H., Kim, S.-E., Ahn, H., Oh, J. & Kim, H. (2003) Analysis of a jet-controlled high-lift hydrofoil with a flap. *Ocean Engineering* 30,16, pp. 2117–2136, doi: 10.1016/S0029-8018(03)00071-4.

29. Sacher, M., Durand, M., Berrini, É., Hauville, F., Duvigneau, R., Le Maître, O. & Astolfi, J.A. (2018) Flexible hydrofoil optimization for the 35th America's Cup with constrained EGO method. *Ocean Engineering* 157, pp. 62–72.

30. Wang, D.X. & He, L. (2010) Adjoint aerodynamic design optimization for blades in multistage turbomachines – Part I: Methodology and verification. *Journal of Turbomachinery* 132 (2), 021011, doi: 10.1115/1.3072498.

31. Wang, X., Song, B., Wang, P. & Sun, C. (2017) Hydrofoil optimization of underwater glider using Free-Form Deformation and surrogate-based optimization. *International Journal of Naval Architecture and Ocean Engineering* 10 (6), pp. 730–740, doi: 10.1016/j.ijnaoe.2017.12.005.

32. Zanette, J., Imbault, D. & Tourabi, A. (2010) A design methodology for cross flow water turbines. *Renewable Energy* 35 (5), pp. 997–1009, doi: 10.1016/j.renene.2009.09.014.

33. Zhang, J., Yang, S. & Liu, J. (2018) Numerical investigation of a novel device for bubble generation to reduce ship drag. *International Journal of Naval Architecture and Ocean Engineering* 10 (5), pp. 629–643.